24th COBEM - 2017

24th ABCM International Congress of Mechanical Engineering
December 3-8, 2017, Curitiba, PR, Brazil

COBEM-2017-1416
COMBINING SHAPE MEMORY ALLOY WIRE ACTUATORS WITH PERMANENT MAGNETS FOR A MULTI-STABLE SMART STRUCTURE

Thiago de P. Sales
School of Mechanical Engineering, Federal University of Uberlândia, Av. João Naves de Ávila, 2121, Building 1M, Uberlândia, MG, Brazil, ZIP 38408-902
thiago.sales@ufu.br

Domingos A. Rade
Department of Mechanical Engineering, Technological Institute of Aeronautics, CTA/ITA/IEM, Pça. Mal. Eduardo Gomes, 50, São José dos Campos, SP, Brazil, ZIP 12228-900
rade@ita.br

Daniel J. Inman
Aerospace Engineering Department, University of Michigan, FXB Building, 1320 Beal Avenue, Ann Arbor, MI, USA, ZIP 48109-2140
daninman@umich.edu

Abstract. *Shape memory alloy (SMA) materials have received attention in recent years as they can be used as thermo-mechanical actuators that have high energetic density and large recoverable strains. SMA wires can be embedded in other components, resulting in compact designs, while also being able to act as load bearing components, thus allowing for weight reduction. Nevertheless, SMAs suffer from low energy conversion efficiency, because of their thermo-mechanical nature. To mitigate this issue, multi-stable arrangements can be adopted, in which actuators benefit from larger off-times, while the system is still capable of maintaining its configuration with no additional energy expense. Following this reasoning, the simultaneous use of SMA wire actuators and permanent magnets is investigated for achieving multi-stable smart structures. A cantilever beam is considered, to which antagonistic SMA wires and permanent magnets are attached to. A numerical modeling procedure is developed accounting for the thermo-mechanical coupling involved in the shape memory effect, the nonlinear electromagnetic interactions, and contact forces. Numerical simulations are performed, and experimental data is used to validate the adopted modeling strategies. Results demonstrate the efficiency of the combination between SMAs and permanent magnets in achieving multi-stable configurations in the context of smart structures.*

Keywords: *shape memory alloys, permanent magnets, multi-stability, smart materials*

1. INTRODUCTION

Smart materials are able to convert energy from one physical domain to another, and, as long as one of these is the mechanical one, they can be adopted as sensors and/or actuators (Leo, 2007). Examples include piezoelectric materials, which exhibit electromechanical coupling; and shape memory alloys (SMAs), which are characterized by their thermomechanical nature. Smart materials can be adopted to enhance traditional mechanical designs by enabling embedded sensing and actuation, leading to compact systems. Furthermore, smart material actuators usually can bear structural loads, and thus promote an overall weight minimization for the system in which they are integrated.

SMAs, in particular, have been largely adopted in applications related to the biomedical, aerospace, and robotics research fields (Petrini and Migliavacca, 2011; Hartl and Lagoudas, 2007; Kheirikhah *et al.*, 2010). Broader review publications on the subject of SMA actuators can also be found (e.g. Mohd Jani *et al.*, 2014), whilst morphing aircraft applications have been considered by Barbarino *et al.* (2014). Table 1 compares the characteristics of several actuators adopted in engineering applications, including SMAs and piezoelectric materials. From it, one can see that NiTi SMAs are the obvious choice when actuators that provide significant displacements and forces are needed, with no critical requirements for short response time or high efficiency (Mohd Jani *et al.*, 2014).

In this respect, the poor energetic efficiency of SMAs can be particularly troublesome. For instance, in the case of SMA-driven morphing technologies, as Barbarino *et al.* (2014) point out, system-level benefits should be expected as long as power consumption can be kept low. In this regard, avoiding continuous actuation of an SMA material consists in an interesting strategy, if this is indeed possible from an operational point of view. Following this reasoning, the adoption of multistable SMA actuation arrangements can lead to significant benefits in terms of energy savings, while still allowing

Table 1. Comparison of actuator performance (Mohd Jani *et al.*, 2014)

Actuator type	Stress [MPa]	Strain [%]	Efficiency [%]	Bandwidth [Hz]	Work per Vol. [J/cm^3]	Power per Vol. [W/cm^3]
NiTi SMAs	200	10	3	3	10	30
Piezoceramics	35	0.2	50	5000	0.035	175
Single crystal piezoelectric	300	1.7	90	5800	2.55	15000
Human muscle	0.007–0.8	1–100	35	2–173	0.035	0.35
Hydraulic	20	50	80	4	5	20
Pneumatic	0.7	50	90	20	0.175	3.5

the system to assume distinct configurations.

Indeed, several morphing aircraft research have pointed towards the use of multistable structures. For the most part, they rely on bistable laminated composites that are actuated by piezoelectric materials (e.g. Lee *et al.*, 2017) or SMA actuators (Lee *et al.*, 2014). In these cases, multistability arises due to unsymmetric lay-up patterns; or results from residual stresses that are introduced during the manufacturing process of the composite part (Hufenbach *et al.*, 2002).

Another means for achieving multistability consists in the use of permanent magnets, as previously demonstrated in the literature (e.g. Zhao *et al.*, 2013, 2015). Permanent magnets already have been adopted in other smart material-related applications, more prominently in vibration energy harvesters (c.f. Karami *et al.*, 2011; Harne and Wang, 2013). Their use in providing multistability allows for structure simplicity, since multiple equilibrium configurations can be achieved within the structural range of motion through nonlinear magnetic-mechanical interactions (Zhao *et al.*, 2015).

When it comes to SMA actuated systems for morphing aircraft applications, multistability has been adopted while considering bistable structural arrangements, as reported by (Barbarino *et al.*, 2014). To the authors' best knowledge, multistability driven by permanent magnets combined with SMA actuation has been considered previously only in applications such as microvalves, microswitches and microactuators (e.g. Barth *et al.*, 2012) and not for structural morphing purposes.

Considering the background given previously, the objective of this paper resides in investigating the simultaneous use of SMA wire actuators with permanent magnets to attain multistable smart structures, as these might be of interest for morphing applications. Following next, an overview of mathematical tools used to perform numerical simulations is presented in Section 2. The setup and procedures adopted for experimental and numerical analysis are then detailed in Section 3. Afterwards, results and discussions are considered in Section 4. Conclusions are finally provided in Section 5.

2. MATHEMATICAL MODELING

The type of system one is interested in is schematic illustrated in Fig. 1. It possesses permanent magnets that interact between themselves, SMA wires that are used as actuators, as well as some sort of stiffness. Another modeling procedure that needs to be taken into account is contact simulation, as the loads that happen between permanent magnets may lead to such condition. In view of conciseness, only a brief overview is provided for the methods adopted for simulation.

2.1 Nonlinear Beam Finite Element Model

To deal with structural modeling, a 2D nonlinear beam finite element (FE) model is considered. It is based on the geometrically nonlinear Reissner beam theory, and further details concerning the formulation can be obtained by consulting the literature (Wriggers, 2008).

The hypotheses of the model are that (i) deformations are confined to the plane on which the beam initially lies upon; (ii) plane cross-sections remain plane after deformation; and (iii) initially, the beam is straight. The beam deformation is schematically shown in Fig. 2, together with the vector basis $(\mathbf{i}_1, \mathbf{i}_2)$, related to the beam local coordinate system. The deformed position (x_1, x_2) of a material point can be computed through:

$$x_1 = X_1 + u_1(X_1) - X_2 \sin\big[\psi(X_1)\big] \qquad \text{and} \qquad x_2 = u_2(X_1) + X_2 \cos\big[\psi(X_1)\big], \tag{1}$$

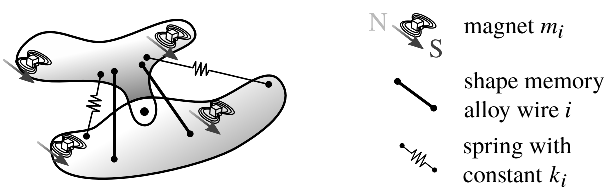

Figure 1. Schematic illustration of a generic system containing permanent magnets and SMA wires

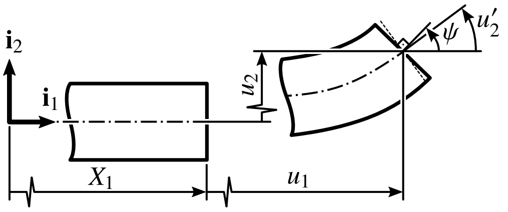

Figure 2. Deformation experienced by a beam according to Reissner theory

where (X_1, X_2) defines its undeformed position, and u_1, u_2, and ψ are the longitudinal, transversal, and rotational displacement fields, respectively. FE discretization is performed for the latter, for $0 \leq X_1^{(e)} \leq L^{(e)}$, such that:

$$\left[u_1^{(e)} \quad u_2^{(e)} \quad \psi^{(e)}\right]^{\mathrm{T}} = \sum\nolimits_{k=1}^{n^{(e)}} \left\{ \left[N_k^{(e)}\left(X_1^{(e)}\right)\mathbf{I}_3\right] \left[(u_1)_k^{(e)} \quad (u_2)_k^{(e)} \quad \psi_k^{(e)}\right]^{\mathrm{T}} \right\} = \mathbf{N}^{(e)}\mathbf{u}^{(e)}, \tag{2}$$

where $\mathbf{I}_3$ denotes a 3×3 identity matrix, $\mathbf{N}^{(e)} \in \mathbb{R}^{3\times 3n^{(e)}}$ is the FE interpolation matrix,

$$\mathbf{u}^{(e)} = \left[(u_1)_1^{(e)} \quad (u_2)_1^{(e)} \quad \psi_1^{(e)} \quad \cdots \quad (u_1)_{n^{(e)}}^{(e)} \quad (u_2)_{n^{(e)}}^{(e)} \quad \psi_{n^{(e)}}^{(e)}\right]^{\mathrm{T}} \tag{3}$$

is the FE nodal degrees-of-freedom (DOFs) vector, and $n^{(e)}$ is the number of nodes of the element. Superscript $(\;)^{\mathrm{T}}$ is used to indicate matrix transposition, superscript $(\;)^{(e)}$ indicates element-related quantities, and subscript $(\;)_k$ allows for distinction between nodes. The undeformed beam element length is $L^{(e)}$, and the shape functions $N_k^{(e)}$, $k = \{1, \ldots, n^{(e)}\}$, are chosen based on the isoparametric FE formulation (Wriggers, 2008).

Strains can be obtained from Eq. (1), whilst stresses are derived based on a linear elastic constitutive law. The nonlinear algebraic equilibrium equations at the element level can then be obtained by considering the Principle of Virtual Work. By adopting the total Lagrangian approach, it is possible to obtain:

$$\mathbf{R}^{(e)} = \mathbf{F}_{\text{int}}^{(e)} - \mathbf{F}_{\text{ext}}^{(e)} = \mathbf{0}, \tag{4}$$

where $\mathbf{F}_{\text{int}}^{(e)}$ and $\mathbf{F}_{\text{ext}}^{(e)}$ are the vectors of internal and external loads, respectively, given by:

$$\mathbf{F}_{\text{int}}^{(e)} = \int_0^{L^{(e)}} \mathbf{B}^{(e)\mathrm{T}}\mathbf{S}^{(e)}\mathrm{d}X_1^{(e)} \qquad \text{and} \qquad \mathbf{F}_{\text{ext}}^{(e)} = \int_0^{L^{(e)}} \mathbf{N}^{(e)\mathrm{T}}\left[n \quad q \quad m\right]^{\mathrm{T}}\mathrm{d}X_1^{(e)}, \tag{5}$$

in which $\mathbf{S}^{(e)}$ is the vector of stresses, $\mathbf{B}^{(e)} = \mathbf{B}^{(e)}\big(\mathbf{u}^{(e)}\big)$ is the strain-displacement matrix, and $n = n\big(X_1^{(e)}\big)$, $q = q\big(X_1^{(e)}\big)$, and $m = m\big(X_1^{(e)}\big)$ are the applied axial, shear, and moment distributed loads. Global equations follow by making use of traditional FE techniques, based on connectivity of the model DOFs.

2.2 Shape Memory Alloy Thermomechanical Model

Complete modeling of the behavior of SMAs is rather challenging, as can be seen from the literature (e.g. Cisse *et al.*, 2016a,b). Here one considers the approach put forward by Chang *et al.* (2006), which is able to represent both shape memory effect, and pseudo-elastic behaviors. An SMA wire actuator is considered, for which gradients along its length are neglected. The stress-strain constitutive law is given by:

$$\sigma = E(\boldsymbol{\xi})[\epsilon - (\xi_1 - \xi_2)\beta], \tag{6}$$

where $\epsilon = \epsilon(t)$ is the strain; $\xi_1 = \xi_1(t)$ and $\xi_2 = \xi_2(t)$ are the volumetric phase fractions of tensile and compressive martensite variants, respectively; $T = T(t)$ is the temperature; and t denotes time. Furthermore, $E(\boldsymbol{\xi}) = E_A + (\xi_1 + \xi_2)\Delta E$, with $\boldsymbol{\xi} = \left[\xi_1 \quad \xi_2\right]^{\mathrm{T}}$, and $\Delta E = E_M - E_A$, where E_A and E_M are the austenite and martensite stiffness moduli, respectively. Finally, β is the stress-free transformation strain.

The martensite fractions evolve according to a piecewise linear kinetic law, i.e.

$$\dot{\boldsymbol{\xi}} = \begin{cases} \nu_0(\boldsymbol{\mu}^{\mathrm{T}}\mathbf{m} - \mu_c)\mathbf{m} & \text{if } \boldsymbol{\mu}^{\mathrm{T}}\mathbf{m} > \mu_c; \\ \mathbf{0} & \text{otherwise,} \end{cases} \tag{7}$$

where $\boldsymbol{\mu}$ is the vector of thermodynamic driving forces, and μ_c is a critical value based on which hysteretic phase transformation takes place. The parameter ν_0 is used to control the speed with which transformation occurs. Vector $\mathbf{m}$ gives the direction along which transformation happens in the (ξ_1, ξ_2) space (c.f. Chang *et al.*, 2006).

Assuming that the SMA wire actuator has undeformed length L_0 and diameter d_0, energy conservation yields:

$$\rho c_0 A_0 L_0 \dot{T} = \rho A_0 L_0 (\boldsymbol{\mu} - T\partial\boldsymbol{\mu}/\partial T)^{\mathrm{T}}\dot{\boldsymbol{\xi}} - h\pi d_0 L_0 (T - T_\infty) + P_E, \tag{8}$$

where $A_0 = \pi d_0^2/4$, h is the convective film coefficient, T_∞ is the ambient temperature, and P_E is the power input term (Chang *et al.*, 2006). The wire is assumed to be heated through Joule effect.

Mechanical equilibrium, on the other hand, can be established by coupling the SMA actuator with the structural FE model equations. For this, one recognizes that:

$$\epsilon = (L - L_0)/L_0 \qquad \text{and} \qquad F_{\text{SMA}} = \sigma A_0, \tag{9}$$

where L denotes the SMA wire actuator instantaneous length, which is dependent on FE DOFs after coupling is considered. The actuator force is denoted by F_{SMA}, and must be applied, accordingly, to the FE nodes that participate in the coupling procedure (Sales, 2017).

2.3 Interacting Permanent Magnets Model

Closed-form analytical solutions for the loads that occur between moving, interacting magnets are not available, and must be pursued numerically, as the magnets are prone to changes in relative orientation (Montalvo, 2014).

To derive expressions for the resulting forces and moments, it is first noted that the force acting on a differential element of volume $\mathrm{d}V_{m_2}$ of a magnet m_2, due to the magnetic field of a magnet m_1, can be evaluated through:

$$\bar{\mathbf{F}}_{m_2,m_1} = \boldsymbol{\nabla}\big(\mathbf{B}_{m_2}^{\mathrm{T}}\mathbf{H}_{m_1}\big), \tag{10}$$

where $\mathbf{B}_{m_2}$ is the residual magnetization of magnet m_2, $\mathbf{H}_{m_1}$ is the magnetic field produced by magnet m_1, and $\boldsymbol{\nabla}$ is the nabla operator. One assumes that $\mathbf{B}_{m_2}$ is constant in the reference frame associated with magnet m_2. With respect to $\mathbf{H}_{m_1}$, it can be computed, in the reference frame related to magnet m_1, from expressions presented by Yonnet and Allag (2009).

The total force and moment acting on magnet m_2 due to magnet m_1 can then be computed from:

$$\mathbf{F}_{m_2,m_1} = \int_{V_{m_2}} \bar{\mathbf{F}}_{m_2,m_1}\mathrm{d}V_{m_2} \qquad \text{and} \qquad \mathbf{M}_{m_2,m_1} = \int_{V_{m_2}} \mathbf{r}\times\bar{\mathbf{F}}_{m_2,m_1}\mathrm{d}V_{m_2}, \tag{11}$$

where vector $\mathbf{r}$ denotes the position of a point in V_{m_2} with respect to the center of mass of magnet m_2, and × designates vector cross-product. Integrals shown in Eq. (11) cannot be evaluated analytically, since $\bar{\mathbf{F}}_{m_2,m_1}$ depends on the relative orientation between magnets m_2 and m_1. Gauss-Legendre quadrature is then adopted (Sales, 2017).

The formulation considers that permanent magnets interact in pairs. If more than two magnets are to be accounted for, the total loads that result from their interactions can be obtained by invoking linear superposition.

2.4 Finite Element Node-to-Element Contact Model

To account for contact conditions during simulations, an algorithm that deals with the case of node-to-element contact, based on inequality constraint functions, has been considered. Complete formulation is presented by Eterovic and Bathe (1991); Bathe and Bouzinov (1997).

The vector containing the loads due to the surface tractions that happen on body b_2 due to the contact between bodies b_1 and b_2 is denoted by $\mathbf{f}_{b_1,b_2}$. It can be expressed in terms of its normal and tangent contributions :

$$\mathbf{f}_{b_1,b_2} = \lambda\hat{\mathbf{n}} + \tau\hat{\mathbf{s}}, \tag{12}$$

where λ and τ are the amplitudes of its normal and tangent components, respectively, and unit vectors $\hat{\mathbf{n}}$ and $\hat{\mathbf{s}}$ are normal and tangent to the target contact surface, respectively.

The gap function g can be computed by (Eterovic and Bathe, 1991):

$$g(\mathbf{x},t) = [\mathbf{x}-\mathbf{y}^*(\mathbf{x},t)]^{\mathrm{T}}\hat{\mathbf{n}}\big(\mathbf{y}^*(\mathbf{x},t)\big), \tag{13}$$

where $\mathbf{x}$ is the location of a point on the contactor surface ∂V_{b_2}, and $\mathbf{y}^*$ is defined as the closest location on the target surface ∂V_{b_1} with respect to the selected point $\mathbf{x}$. Normal contact conditions can then be expressed in terms of the constraints:

$$g \geq 0\,, \qquad \lambda \geq 0 \qquad \text{and} \qquad g\lambda = 0. \tag{14}$$

Friction during contact can be considered by means of Coulomb's law. For this purpose, the normalized variable $\bar{\tau} \equiv \tau/(\mu_f\lambda)$ is considered, where μ_f is the coefficient of friction between ∂V_{b_1} and ∂V_{b_2}.

The magnitude of the relative tangential velocity $\dot{u}$ between the contacting surfaces can be obtained from:

$$\dot{u}(\mathbf{x},t) = \big[\dot{\mathbf{u}}_{b_2}\big(\mathbf{y}^*(\mathbf{x},t),t\big) - \dot{\mathbf{u}}_{b_1}(\mathbf{x},t)\big]^{\mathrm{T}}\hat{\mathbf{s}}\big(\mathbf{y}^*(\mathbf{x},t)\big), \tag{15}$$

where $\dot{\mathbf{u}}_{b_i}$ is the velocity of a point on ∂V_{b_i}, $i = \{1,2\}$. Coulomb's law of friction then implies:

$$|\bar{\tau}| \leq 1 \qquad \text{such that:} \qquad |\bar{\tau}| < 1 \quad \Rightarrow \quad \dot{u} = 0\,, \qquad |\bar{\tau}| = 1 \quad \Rightarrow \quad \mathrm{sgn}(\dot{u}) = \mathrm{sgn}\,(\bar{\tau})\,. \tag{16}$$

To incorporate the constraints given in Eq. (14) in FE formulations, a function $w_n(g,\lambda)$ can be defined such that $w_n = 0$ implies the relations in Eq. (14). Based on regularization of the constraints, a suitable expression for w_n is:

$$w_n(g,\lambda) = (g+\lambda)/2 - [(g-\lambda)^2/4 + \epsilon_n]^{1/2}, \tag{17}$$

where $\epsilon_n \ll 1$. The same procedure can be adopted for the friction-related constraints given in Eq. (16). The following implicit definition is made for $w_s = w_s(\dot{u},\bar{\tau})$:

$$\bar{\tau} + w_s - 2/\pi\tan^{-1}\{(\dot{u}-w_s)/\epsilon_s\} = 0, \tag{18}$$

such that Eq. (16) becomes approximately satisfied when $w_s = 0$, for $\epsilon_s \ll 1$.

The contact loads acting on a FE contactor node k_c and on target element nodes k_1 and k_2, for the case of a target FE with only two nodes, can be computed as:

$$\mathbf{F}_{\text{contact},k_c} = -\lambda(\hat{\mathbf{n}} + \mu_f \bar{\tau}\hat{\mathbf{s}}), \qquad \mathbf{F}_{\text{contact},k_1} = \left(1 - \bar{\beta}\right)\lambda(\hat{\mathbf{n}} + \mu_f \bar{\tau}\hat{\mathbf{s}}) \qquad \text{and} \qquad \mathbf{F}_{\text{contact},k_2} = \bar{\beta}\lambda(\hat{\mathbf{n}} + \mu_f \bar{\tau}\hat{\mathbf{s}}), \tag{19}$$

respectively, where $\bar{\beta}$ is a weighting parameter used for locating $\mathbf{y}^*$ (Eterovic and Bathe, 1991; Sales, 2017).

Based on previous considerations, contact conditions can be incorporated into a FE formulation through: (i) the application of the contact forces to the relevant FE DOFs; and (ii) the enforcement of the constraints w_n and w_s.

2.5 Solution Procedures

The modeling techniques described in the previous Subsections were combined into a single simulation framework, developed in the MATLAB® programming environment. Coupling was considered between the FE model, SMA wire actuators, interacting permanent magnets and contact pairs, as can be seen in the simplified block diagram for the implemented model, shown in Fig. 3.

The complete model consists in a set of nonlinear algebraic equations. These were solved by making use of the Newton-Raphson algorithm combined with a line search method. Numerical smoothing techniques were also adopted for addressing convergence issues related to discontinuities observed in the model. A more complete description of the adopted procedures is provided by Sales (2017).

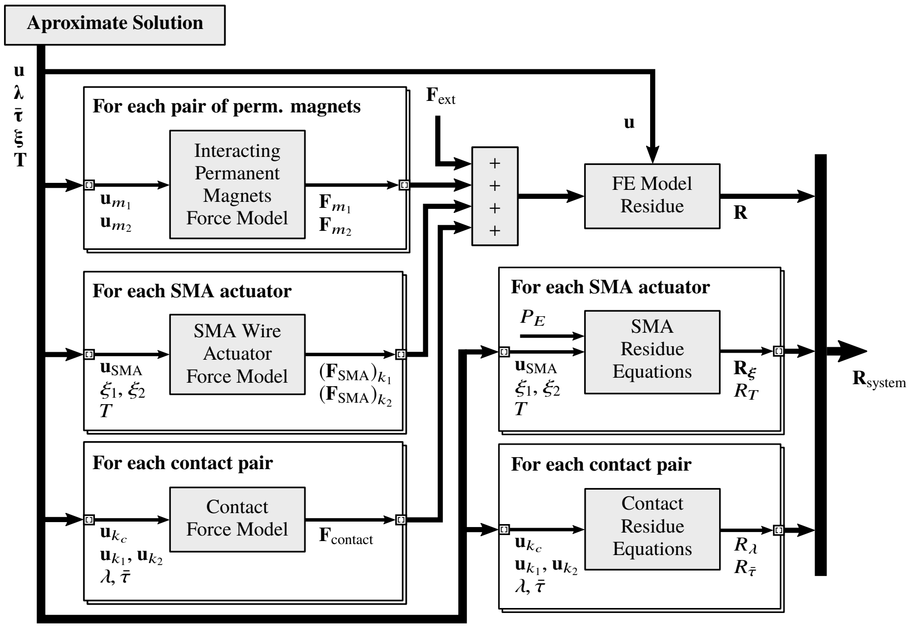

Figure 3. Simplified block diagram for the implemented model

3. EXPERIMENTAL AND NUMERICAL SETUPS

3.1 System description

To evaluate the simultaneous use of SMA wire actuators with permanent magnets as a means to attain multistable smart structures, as proposed in Section 1, one considers the system shown in Fig. 4. It consists of a thin aluminum clamped-free beam, with two antagonistic SMA wire actuators (Muscle Wires® Flexinol 300 LT) attached to it. N52 grade NdFeB permanent magnets were added near the end of the beam, and secured with the use of Loctite® Super Glue. Identical magnets have been kept stationary, positioned to allow for the desired behavior for the system.

Table 2 provides the values of the coordinates of the points identified in Fig. 4(a). The beam width and thickness are oriented along X_3 and X_1, and measure 28.5 mm and 1.2 mm, respectively. The diameter of the SMA wires is equal to 300 µm, and the permanent magnets have sides measuring 6.35 mm. Components are arranged symmetrically with respect to the (X_1, X_2) and (X_2, X_3) planes when the beam occupies a vertical position.

SMA wires have been installed as received from the manufacturer. They were routed through small pulleys, as can be seen in Fig. 5. Considering their total length, and that only three pulleys were used in the setup, the effect of the latter is deemed negligible. Before securing the wires, a static pre-load of $\sigma_0 = 100$ MPa was applied with the use of dead weights.

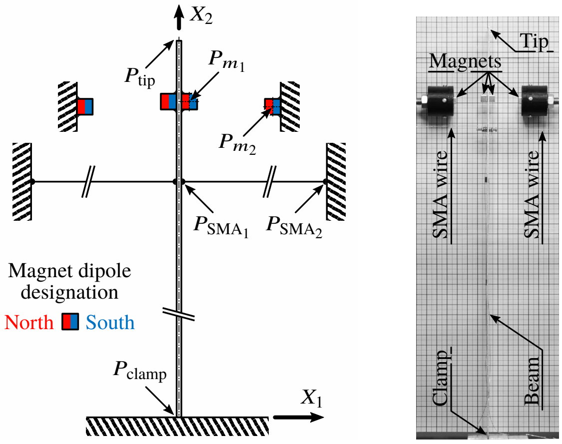

(a) Schematic drawing (b) System photograph

Figure 4. System considered for testing

Table 2. Coordinates of the points identified in Fig. 4(a)

Point	X_1 [mm]	X_2 [mm]
P_{clamp}	0.0	0.0
P_{tip}	0.0	400.0
P_{m_1}	3.775	330.0
P_{m_2}	34.0	328.0
P_{SMA_1}	4.775	300.0
P_{SMA_2}	1314.775	300.0

3.2 Experimental Setup

During tests, each SMA wire actuator was subjected to its corresponding voltage loading pattern, as shown in Fig. 6. As can be seen, a ramp loading/unloading condition is considered for each wire, with only one of them being actuated at a time. It is also possible to verify that quasi-static loading conditions have been considered, so issues related to SMA rate-dependency (Cisse *et al.*, 2016b) would be avoided.

Two system configurations have been investigated, in which permanent magnets were and were not incorporated to the system. Tests were performed with room temperature equal to 20 °C, maintained by an air conditioning unit. Acquisitions and recordings were made with the help of a National Instruments® USB-6259 BNC DAQ device, and a personal laptop.

Temperatures, voltages and currents have been monitored on both SMA wires. Temperatures were measured with Omega® K type thermocouples, with 80 µm in diameter, paired with Analog Devices® AD8495 precision amplifiers. Voltage drops along each of the actuators have been measured with the help of simple voltage dividers. Currents applied to the wires have been recorded with Texas Instruments® INA250 integrated circuits.

The displacement field of the beam was captured with a Canon® EOS 1000D camera, coupled to a EF75–300mm f/4-5.6 lens. Photos were taken every 5 seconds, which is consistent with the adopted quasi-static SMA actuation pattern. Acquired images were post-processed, and displacements have been determined with the use of the open-source Tracker software (Brown, 2017).

The command voltage used to drive the SMA actuators was generated by the NI® USB-6259 BNC DAQ, and routed to a Labworks Inc. PA-138 Linear Power Amplifier, with a gain of approximately 29 V/V. A relay was used to switch the electrical current between the left and right actuators, as needed.

3.3 Numerical Setup

The finite element mesh adopted for numerical simulations is shown in Fig. 7. The beam was discretized with 40 elements with three nodes each. FEs with two nodes each were used to connect the SMA wire actuators and permanent magnets coupling nodes to the beam mesh, and simultaneously account for small offsets observed in the experimental

Figure 5. Photograph of the system before installation of magnets

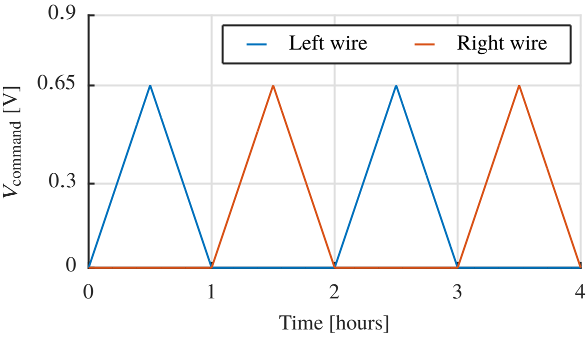

Figure 6. Voltages adopted for driving the SMA wire actuators

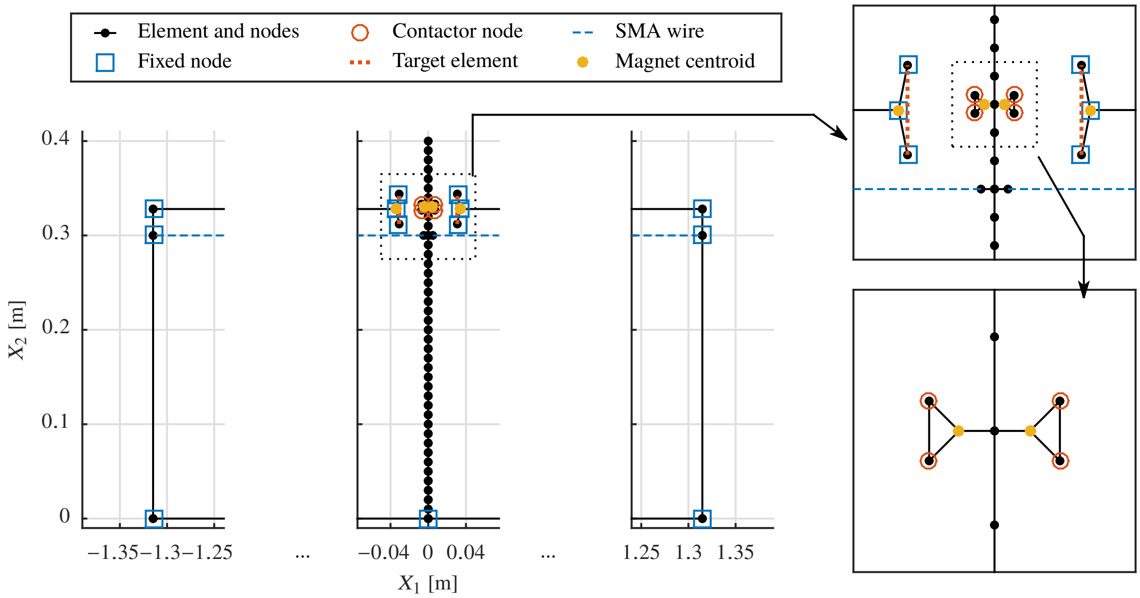

Figure 7. Finite element mesh used for numerical simulations

setup (cf. zoomed plots shown in Fig. 7). FEs with two nodes each were also considered for modeling the surfaces of the magnets that experience contact.

Values of the parameters used for numerical simulations are not provided here due to space limitations, but can be found in (Sales, 2017). One remarks that the power input term P_E [see Eq. (8)] was determined from experimental data recordings for each SMA wire actuator. The ambient temperature T_∞ was set equal to 20 °C, as adopted during experiments. The convection film coefficient h was determined by considering the relationship between T and P_E.

Characterization of the SMA wire actuators was not performed prior to the tests reported herein. Because of this, the values adopted in simulations for SMA actuators' parameters have been obtained from a mix of literature data (e.g. DYNALLOY, 2017), and fitted parameters. The latter were obtained as the solution to an inverse identification problem, by considering the minimization of the RMS deviation between the model and experimental beam displacement at the SMA actuators attachment location (Sales, 2017).

4. RESULTS AND DISCUSSION

Results are now provided. Figure 8 shows a comparison between the experimental beam tip displacements for the system with and without permanent magnets. The time labels provided in this figure serve as references for the pictures of the system given in Fig. 9, from which the complete displacement field of the beam can be seen.

For the analysis of the time history curves given here, one highlights that results corresponding to the second and subsequent actuation cycles are plotted by considering different time references, in view of the actuation voltage pattern, which has a period of 2 hours (c.f. Fig. 6). As an example, displacements corresponding to time instants between 2 and 4 hours are plotted as if they have occurred during the 0 to 2 hours time frame. Because of this, results overlap. Furthermore, because the beam was close to a vertical position in the initial system configurations, distinct displacement paths can be seen for the initial 0.33 h in Fig. 8. An indication of this is provided, and the same holds for other time history plots.

Line thicknesses used in the plots have been chosen to represent the maximum uncertainty associated with measure-

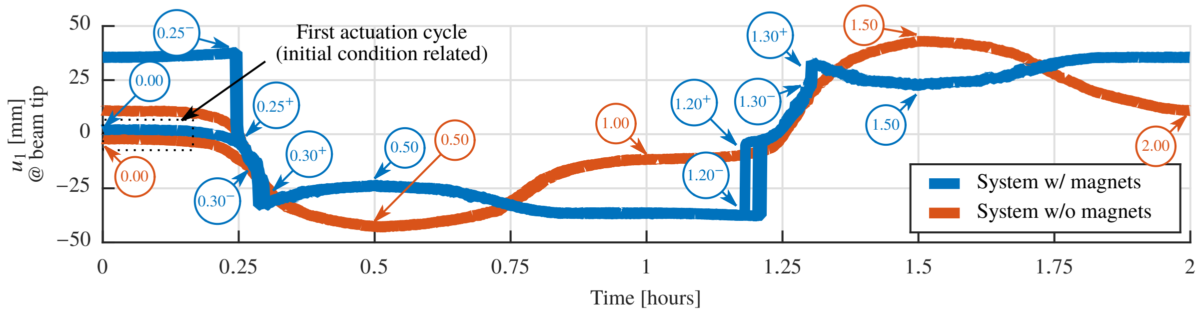

Figure 8. Experimentally measured beam displacements for the system with and without magnets

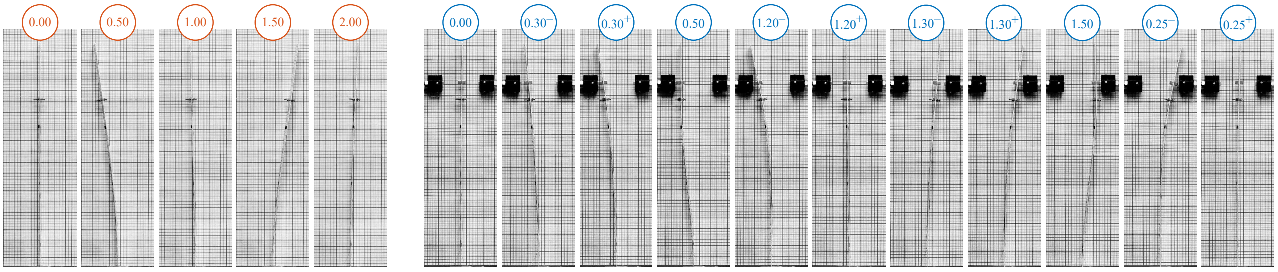

(a) System without magnets

(b) System with magnets

Figure 9. System under test, at different actuation conditions, labeled according to time, in hours, cf. Fig. 8

ments. In the case of displacements, uncertainty is due to the use of an image tracking software for their computation.

Figure 8 immediately shows that permanent magnets are able to provide two new equilibrium configurations for the tested system. These are virtually similar to the configurations identified by the labels 1.20^- and 0.25^- in Fig. 9(b).

Figures 8 and 9 also indicate that larger displacements are achieved by the system without permanent magnets. This is due to the positions used for placement of the magnets: when a pair gets in contact, the motion of the beam is effectively constrained. Nevertheless, in an actual use-case, actuation would be seized after the system moved to one of its stable configurations. Subsequent actuation could still be used for stiffness control, but is not required otherwise.

Chronologies of the experiments are now provided. The one without permanent magnets is considered first. Labels used in the description refer to Fig. 9(a). The system departs from its initial condition, labeled 0.00. The left actuator is heated through Joule effect. Phase transformation starts, and the wire contracts. Simultaneously, the right wire gets tensioned. Therefore, tension on the left wire also rises. The SMA transformation temperature then increases as it contracts. Maximum tip displacement is achieved, labeled 0.50. Following, the left actuator has its temperature decreased. The beam moves towards its initial position, and ends up in a slightly offset condition, labeled 1.00. An analogous procedure is used for the right actuator. It gets heated, contracts due to phase transformation, and the left wire gets tensioned. The maximum displacement configuration is eventually reached, labeled 1.50. Afterwards, the right SMA length increases, while the tension on the left wire reduces, because voltage drops. The condition labeled 2.00 is then achieved. Another actuation cycle starts, and the system successively moves through the states labeled 0.50, 1.00, 1.50, and 2.00. The offsets observed for the configurations labeled 1.00 and 2.00 are most likely due to insufficient initial pretension of the SMA wires (such that martensite reorientation was not fully achieved during setup). This behavior is explained, for instance, by Sofla *et al.* (2008), who explored it for two-way antagonistic actuation while using one-way SMAs.

The timeline for the experiments performed with the system with permanent magnets is similar to the one described previously. Labels now refer to Fig. 9(b). The system was initially as shown in label 0.00. The left wire was heated, and contracted due to phase transformation. After 18 minutes of testing, the system experienced a snap-through, induced by close proximity of the left pair of permanent magnets. Configurations immediately before and after magnets' contact are labeled 0.30^- and 0.30^+, respectively. Actuation could then be interrupted, and the system would maintain its configuration. Nonetheless, voltage supplied to the left actuator continued to rise, for consistency w.r.t. the test performed without permanent magnets. The beam then deformed as if it was constrained at the location where magnets made contact. Its shape for maximum actuation voltage is labeled 0.50. Voltage provided to the left actuator was then continually reduced, until nullified. The system, nevertheless, maintained its new equilibrium state, which is almost identical to the one labeled 1.20^-. The right wire was actuated subsequently. After enough tension built up due to its contraction, magnets that previously got together were able to separate. Configurations immediately before and after snap-through are labeled 1.20^- and 1.20^+, respectively. Voltage supplied to the right actuator continued to increase, and the system snaped-through one more time, when permanent magnets on the right got too close to each other. The system departed from the configuration labeled 1.30^- to the one labeled 1.30^+. The right wire was still fed with increasing voltage values, until the configuration labeled 1.50 was achieved. Then, the command voltage started reducing, until zeroed. The system was able to maintain a new stable state, with the beam displaced to the right, virtually identical to the one labeled 0.25^-. Afterwards, the second actuation cycle was initiated. Differences w.r.t. the first one are related to the initial condition assumed for the system. While the beam configuration was initially vertical, now it is deformed to the right. Because of this, when the left wire was heated, sufficient tension built up, until the right pair of magnets detached, c.f. labels 0.25^- and 0.25^+. From then onward, events considered previously repeated, as seen through overlapping curves in Fig. 8.

Figure 10 compares numerical and experimental beam tip displacements for the system without permanent magnets, while Fig. 11 shows power versus displacement hysteresis loops for the same experimental condition. As can be seen, the beam tip displacement given by the numerical model is in good agreement with experimental data, both qualitatively and quantitatively. Few differences can be observed during SMA actuation, and are related to the phase transformation law assumed by the adopted model. Plots given in Fig. 11 show that the adopted SMA model predicts hysteresis related to the shape memory effect reasonably well. Transformation smoothing techniques and proper characterization of the SMA

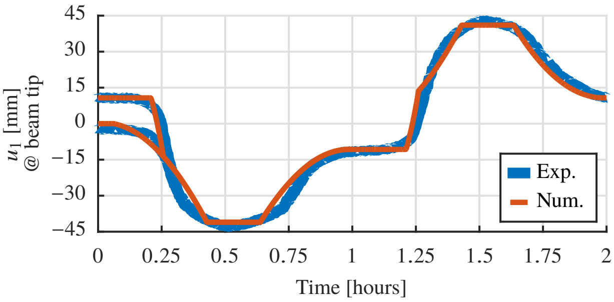

Figure 10. Experimental and numerically computed beam tip displacement for the system without magnets

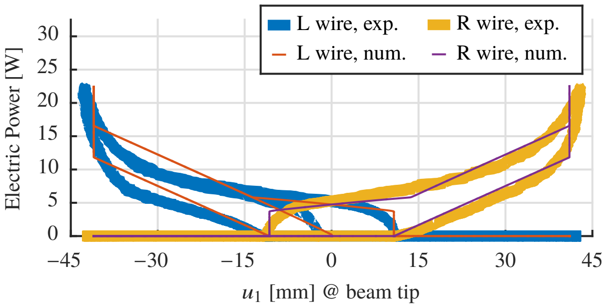

Figure 11. Comparison of electric power–displacement hysteresis loops for the system without magnets

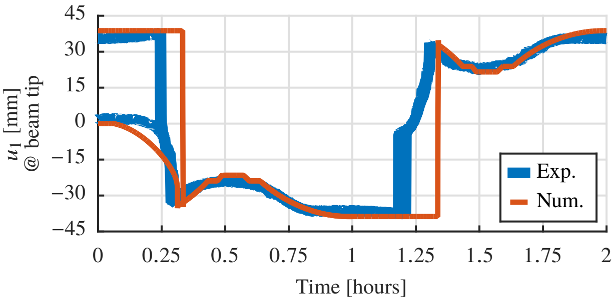

Figure 12. Experimental and numerically computed beam tip displacement for the system with magnets

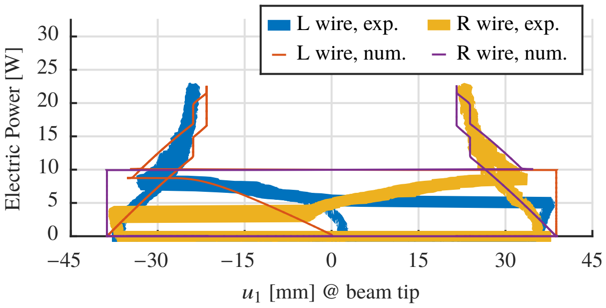

Figure 13. Comparison of electric power–displacement hysteresis loops for the system with magnets

actuators could have been adopted for the achievement of better agreement.

Numerical and experimental results related to the condition in which permanent magnets were attached to the system are provided in Figs. 12 and 13, which show time histories of the beam tip displacement, and power versus displacement hysteresis loops, respectively. Fairly good predictions are made by the numerical model for the displacement of the beam tip. An exception can be pointed out for the instants of time at which pair of permanent magnets should separate. Instead of occurring at 0.25 and 1.20 h, as observed during experiments, for the model they happen at 0.3 and 1.3 h, respectively.

Figure 13 shows that the structure is able to stay at deformed configurations without expending external power, as a result of multistability driven by the permanent magnets. The beam tip can be maintained displaced by amounts of approximately ±37 mm. Because of offsets observed during experimental testing, it is also possible for it to be positioned within ±11 mm of tip displacement. These configurations can also be attained by the system without permanent magnets, c.f. Fig. 11. This figure also show that a beam displacement of ±37 mm can only be achieved, for the system without permanent magnets, at the expense of roughly 7 or 12 W, depending on the SMA wire actuator state. If such configuration needs to be maintained for long periods of time, significant energy savings can be obtained by adopting the multistable design.

5. CONCLUSIONS

By considering an illustrative system, in this paper one verified that multistability can be achieved through the simultaneous use of SMA wire actuators and permanent magnets. It was shown that multistable behavior can arise from the interaction between NdFeB magnets. One also verified that SMA actuators were able to move the system between distinct stable configurations it acquired after permanent magnets were added to it. A general numerical modeling procedure was also described. Despite some minor deviations, related to the prediction of times at which permanent magnets that are in contact detach, the model was able to accurately represent the system at hand. Proper experimental characterization of the SMA actuators used in tests might have helped mitigate this issue.

The authors anticipate that the use of the concept considered in this paper for morphing applications has been the subject of research that will be published in due time.

6. ACKNOWLEDGMENTS

The authors are thankful for the financial support provided by the Air Force Office of Scientific Research (AFOSR, grant #FA9550-12-1-0447), and the Brazilian agencies CNPq (grants #162135/2013-0, #402238/2013-3, #310633/2013-3 and #202442/2014-4), CAPES, and FAPESP.

7. REFERENCES

Barbarino, S., Flores, E.I.S., Ajaj, R.M., Dayyani, I. and Friswell, M.I., 2014. "A review on shape memory alloys with applications to morphing aircraft". *Smart Mater. Struct.*, Vol. 23, No. 6, pp. 063001(1)–063001(19).

Barth, J., Megnin, C. and Kohl, M., 2012. "A bistable shape memory alloy microvalve with magnetostatic latches". *J. Microelectromech. Syst.*, Vol. 21, No. 1, pp. 76–84.

Bathe, K.J. and Bouzinov, P.A., 1997. "On the constraint function method for contact problems". *Computers & Structures*, Vol. 64, No. 5–6, pp. 1069–1085.

Brown, D., 2017. "Tracker video analysis and modeling tool". < `http://physlets.org/tracker/` >. Version 4.97, Acessed on: 2017-05-19.

Chang, B.C., Shaw, J.A. and Iadicola, M.A., 2006. "Thermodynamics of shape memory alloy wire: modeling, experiments, and application". *Continuum Mech. Thermodyn.*, Vol. 18, No. 1, pp. 83–118.

Cisse, C., Zaki, W. and Zineb, T.B., 2016a. "A review of constitutive models and modeling techniques for shape memory alloys". *Int. J. Plast.*, Vol. 76, pp. 244–284.

Cisse, C., Zaki, W. and Zineb, T.B., 2016b. "A review of modeling techniques for advanced effects in shape memory alloy behavior". *Smart Mater. Struct.*, Vol. 25, No. 10, pp. 103001(1)–103001(36).

DYNALLOY, 2017. "Technical characteristics of Flexinol® actuator wires". < `http://www.dynalloy.com/pdfs/TCF1140.pdf` >. Acessed on: 2017-07-31.

Eterovic, A.L. and Bathe, K.J., 1991. "On the treatment of inequality constraints arising from contact conditions in finite element analysis". *Computers & Structures*, Vol. 40, No. 2, pp. 203–209.

Harne, R.L. and Wang, K.W., 2013. "A review of the recent research on vibration energy harvesting via bistable systems". *Smart Mater. Struct.*, Vol. 22, No. 2, pp. 023001–1–023001–12.

Hartl, D.J. and Lagoudas, D.C., 2007. "Aerospace applications of shape memory alloys". *Proceedings of the Institution of Mechanical Engineers, Part G: Journal of Aerospace Engineering*, Vol. 221, No. 4, pp. 535–552.

Hufenbach, W., Gude, M. and Kroll, L., 2002. "Design of multistable composites for application in adaptive structures". *Compos. Sci. Technol.*, Vol. 62, No. 16, pp. 2201–2207.

Karami, M.A., Varoto, P.S. and Inman, D.J., 2011. "Experimental study of the nonlinear hybrid energy harvesting system". In *Modal Analysis Topics, Volume 3. Conference Proceedings of the Society for Experimental Mechanics Series*. pp. 461–478.

Kheirikhah, M.M., Rabiee, S. and Edalat, M.E., 2010. "A review of shape memory alloy actuators in robotics". In *RoboCup 2010: Robot Soccer World Cup XIV*. pp. 206–217.

Lee, A.J., Moosavian, A. and Inman, D.J., 2017. "A piezoelectrically generated bistable laminate for morphing". *Mater. Lett.*, Vol. 190, pp. 123–126.

Lee, J.G., Ryu, J., Lee, H. and Cho, M., 2014. "Saddle-shaped, bistable morphing panel with shape memory alloy spring actuator". *Smart Mater. Struct.*, Vol. 23, No. 7, pp. 074013–1–074013–9.

Leo, D.J., 2007. *Engineering analysis of smart material systems*. John Wiley & Sons.

Mohd Jani, J., Leary, M., Subic, A. and Gibson, M.A., 2014. "A review of shape memory alloy research, applications and opportunities". *Materials & Design*, Vol. 56, pp. 1078–1113.

Montalvo, C.J., 2014. *Meta aircraft flight dynamics and controls*. Ph.D. dissertation, School of Aerospace Engineering, Georgia Institute of Technology. Chapter 2, Section 3.

Petrini, L. and Migliavacca, F., 2011. "Biomedical applications of shape memory alloys". *Journal of Metallurgy*, Vol. 2011, pp. 501483(1)–501483(15).

Sales, T.P., 2017. *Simultaneous use of shape memory alloys and permanent magnets in multistable smart structures for morphing aircraft applications*. Ph.D. dissertation, School of Mechanical Engineering, Federal University of Uberlândia.

Sofla, A., Elzey, D. and Wadley, H., 2008. "Two-way antagonistic shape actuation based on the one-way shape memory effect". *J. Intell. Mater. Syst. Struct.*, Vol. 19, No. 9, pp. 1017–1027.

Wriggers, P., 2008. *Nonlinear finite element methods*. Springer-Verlag Berlin Heidelberg. Chapter 9, Section 2.

Yonnet, J.P. and Allag, H., 2009. "Analytical calculation of cuboïdal magnet interactions in 3D". In *Proceedings of LDIA 2009*. pp. 162–165.

Zhao, J., Gao, R., Chen, G., Liu, S., Cao, Q. and Qiu, T., 2015. "Nonlinear coupling mechanical model for large stroke magnetic-based multistable mechanisms". *Mech. Mach. Theory*, Vol. 83, pp. 56–68.

Zhao, J., Gao, R., Yang, Y., Huang, Y. and Hu, P., 2013. "A bidirectional acceleration switch incorporating magnetic-fields-based tristable mechanism". *IEEE/ASME Transactions on Mechatronics*, Vol. 18, No. 1, pp. 113–120.

8. RESPONSIBILITY NOTICE

The authors are the only responsible for the printed material included in this paper.